photonics

MDPI

Article

Spatially Filtered Back Focal Plane Imaging for Directional Fluorescence Lifetime Study of Polaritonic States

Povilas Jurkšaitis [1,*], Justina Anulytė [1], Evita Spalinskaitė [1], Ernesta Bužavaitė-Vertelienė [1,2,*], Vytautas Žičkus [1,3], Ieva Plikusienė [1,2] and Zigmas Balevičius [1]

[1] State Research Institute Center for Physical Sciences and Technology, Savanorių Street 231, LT-02300 Vilnius, Lithuania
[2] NanoTechnas—Center of Nanotechnology and Materials Science, Faculty of Chemistry and Geosciences, Vilnius University, Naugarduko Street 24, LT-03225 Vilnius, Lithuania
[3] School of Physics and Astronomy, University of Glasgow, Glasgow G12 8QQ, UK
* Correspondence: povilas.jurksaitis@ftmc.lt (P.J.); ernesta.verteliene@ftmc.lt (E.B.-V.)

Abstract

Back focal plane (BFP) imaging has emerged as a widely used technique for investigating various nanoscale optical devices. The ability to provide the full angular distribution of emitted light has enabled the engineering of precise radiation patterns, enabling new advances in nanophotonics. Continuous improvements in the BFP imaging technique, including wavelength, polarization, and phase-resolved signal detection, have allowed us to gain crucial insights into the various optical and material properties of nanophotonic devices. In this study, we introduce a fluorescence lifetime-resolved BFP imaging configuration, which uses a spatial filtering technique in the Fourier plane to discriminate between different emission directions. Uniform silver film (45 nm) with a PMMA matrix layer of about 20 nm containing Rhodamine 6G fluorescent molecular dye was prepared and measured using total internal reflection ellipsometry (TIRE). A coupled oscillator model was used, and strong coupling was observed with a coupling strength of 160 meV. Time-correlated single-photon counting was used for the estimation of fluorescence lifetime in the sub-nanosecond regime, and a direction-dependent lifetime was observed in the BFP imaging configuration. This modified fluorescence-lifetime-resolved BFP microscopy method is essential for directly correlating the collective quantum dynamics (lifetime/decay rate) with the far-field radiation pattern (angle/coherence). It offers a critical tool for designing and optimizing quantum nanophotonic devices, such as polariton-based components and highly directional single-photon emitters, where controlling both excited-state dynamics and spatial coherence is paramount.

Keywords: strong coupling; surface plasmon polaritons; spatial filtering; fluorescence lifetime; Rhodamine 6G

Received: 20 October 2025
Revised: 10 November 2025
Accepted: 21 November 2025
Published: 27 November 2025

Citation: Jurkšaitis, P.; Anulytė, J.; Spalinskaitė, E.; Bužavaitė-Vertelienė, E.; Žičkus, V.; Plikusienė, I.; Balevičius, Z. Spatially Filtered Back Focal Plane Imaging for Directional Fluorescence Lifetime Study of Polaritonic States. *Photonics* **2025**, *12*, 1165. https://doi.org/10.3390/photonics12121165

1. Introduction

Recent advances in nanophotonics have led to a wide range of new nanoscale optical devices with applications ranging from spectroscopy, imaging, and nanolasers to quantum optics and sensing [1–5]. A continuous development of optical measurement techniques followed, with back focal plane (BFP) imaging emerging as a widely used technique for the investigation and characterization of nanophotonic devices, as well as microscopy techniques with a wide field of view [6] and spatiotemporal information [7]. BFP imaging offers a simple way of obtaining the full angular distribution of scattered light without the need

to use goniometers [8] or other prism-based devices [9], which turned out to be slow and cumbersome. Single-shot measurements, offered by BFP imaging, provide the opportunity for the real-time investigation of structures [10]. The ability to measure radiation patterns allows us to observe the dipole orientations of single molecules [10,11], which was later followed by the investigation of dipole orientations in various other nanophotonic platforms [12–14]. Thus, BFP imaging enables researchers to engineer nanophotonic devices with precise radiation patterns. The working principles of BFP are based on Fourier optics, particularly on the Fourier transformation properties of a lens. When an object, such as a single particle, is placed on the imaging plane of the objective lens, the output intensity distribution observed on the BFP corresponds to the Fourier transform of the image [15]. This property of the lens translates the spatial distribution of the image into an angular distribution and allows researchers to gain information about the emission and scattering processes. This is especially important when considering scattering phenomena involving metallic nanostructures in weak and strong coupling regimes, for instance, organic dye molecules coupled with Surface Plasmon Polaritons (SPPs).

The successful use of BFP imaging has highlighted a limiting factor of this technique: only the intensity of the light is measured. Improvements to this technique have been introduced through the addition of wavelength [16,17], polarization [16,18], and phase-resolved [19,20] signal detection, enabling new BFP imaging configurations [17,19,21,22].

Fluorescence lifetime remains one of the most important characteristics for describing light-matter interactions in nanophotonic systems. Various structures have been investigated to enable modification of emission properties in the far field. For example, emitters placed in conjunction with plasmonic nanostructures exhibit modified emission [23–28], which is crucial for the investigation of single-photon sources. Such modification of the fluorescence emission and lifetime is the primary signature of the weak coupling regime [29], where the coupling is described as an interaction in which system losses exceed the rate of light-matter interaction.

In contrast, fluorescence lifetime in the strong coupling regime is even further modified by the formation of polaritonic eigenstates [30], providing new possibilities in quantum nanophotonics [31,32] and modified chemical dynamics [33–35]. Strong coupling is defined as $g \gg \gamma_{ex}, \gamma_{spp}$, where γ_{ex} and γ_{spp} are the decay rates of the exciton and plasmon modes, respectively. Polaritonic states are new eigenstates of the system, described as coherent superposition of exciton and photon modes with dispersive characteristics [36].

Additionally, modification of emission and absorption spectra is evident through the emergence of a double-peak structure [30], corresponding to upper polariton (UP) and lower polariton (LP) energies. During strong coupling, exciton and plasmon modes exhibit coherent energy exchange at a rate equal to the Rabi frequency, drastically altering the characteristic lifetime of the system [37,38]. Rabi oscillations in the time domain can be observed by performing complex pump-probe experiments [37]. These temporal features are highly desirable for nanophotonic devices.

The nature of plasmon-exciton polaritonic states, formed by the coherent superposition of many excitons and plasmons, offers a direct link to collective quantum phenomena. When the plasmonic system couples to a large number (N) of closely packed dye molecules (excitons), the resulting polaritons exhibit traits analogous to Dicke superradiance or subradiance [39]. Specifically, the polariton eigenmodes represent collective excitations of the entire ensemble, which can spontaneously decay at rates proportional to N (superradiance, leading to faster decay/shorter lifetime) or become subradiant (leading to slower decay/longer lifetime) depending on the phase-matching of the coupled emitters.

The collective and coherent nature of these polaritonic states also fundamentally dictates the presence of spatial coherence of the emitted light [39,40]. The light radiated

from a polariton mode is intrinsically spatially coherent across the length scale of the polariton wave packet, thus directly influencing the resulting angular emission pattern measured in the BFP. Evaluating the angle-dependent fluorescence lifetime provides a unique path to disentangle these complex coherent decay mechanisms and map the spatial coherence properties of the collective plasmon-exciton modes.

Thus, a modified BFP configuration is introduced by adding a new dimensionality to the widely used BFP imaging method. A combination of spatially filtered BFP and fluorescence lifetime measurement techniques is used to gain additional information about fluorescence lifetimes. Furthermore, this combined knowledge of intensity and fluorescence lifetime data would, in principle, allow the evaluation of energy transfer and quenching regimes [41] in a microscopy setup. Therefore, in this study, we evaluate angular emission properties by using a spatial filtering technique to select different sections of BFP and measure the fluorescence lifetime from areas in the strong coupling regime. This enables the construction of an angle-dependent fluorescence lifetime map, which provides wide-field information in the Fourier plane together with corresponding fluorescence lifetimes. We showcase the applicability of the method using molecular Rhodamine 6G (R6G) fluorescence dye strongly coupled to SPPs, with coupling strengths reaching up to 160 meV.

2. Results

Modification of excited-state dynamics due to coupling to plasmonic modes has been observed in various nanophotonic systems [42–45]. However, direct observation of Rabi oscillations between lower polariton (LP) and upper polariton (UP) states is challenging because of the extremely fast transition times, which are of the order of femtoseconds in plasmonic systems. In our experiments, the structure consisting of a cover slip (CS) coated with silver and PMMA-R6G layer (hereafter referred to as CS/Ag/PMMA-R6G) was measured in a total internal reflection ellipsometry (TIRE) setup to retrieve dispersion relations governed by plasmon–exciton interactions in a multilayered structure (Figure 1A). Since ellipsometry enables measurement of polarization state changes upon reflection, the information about a specific polarization component can be extracted. It is well known that the surface plasmon polariton (SPP) mode can be excited only in p-polarization; therefore, only the p-polarized component of the reflected light (Rp) is relevant for studying strong coupling between SPP and the emitter. The measured Rp of the coupled SPP and R6G polariton state at different angles of incidence is shown in Figure 1B, where the upper and lower polariton branches (marked UP and LP, respectively) as well as the weakly coupled R6G molecule line (red dashed line), can be observed.

These measured UP and LP values were recalculated into wave vectors to obtain the dispersion of the hybrid polaritonic state (shown in Figure 1C as red squares). Coupling between R6G and SPP can be described by a simple coupled oscillator model with Hamiltonian [4]:

$$H = \begin{pmatrix} E_{spp} & g \\ g & E_{ex} \end{pmatrix}$$

where E_{spp} and E_{ex} are uncoupled eigenfrequencies of SPP and R6G exciton, respectively, g is the coupling strength between the excitations. Eigenvalues of the coupled state can be expressed as

$$E_{\pm} = \frac{E_{spp} + E_{ex}}{2} \pm \frac{1}{2}\sqrt{\left(E_{spp} - E_{ex}\right)^2 + 4g^2}$$

Modeled dispersion relation exhibits strong coupling with anticrossing at $k_{\parallel} = 12.5\ \mu m^{-1}$ and $g = 160$ meV (Figure 1C). Ellipsometry measurements of coupled SPP-R6G are in good agreement with the coupled oscillator model, indicating that polaritonic states are present in the sample.

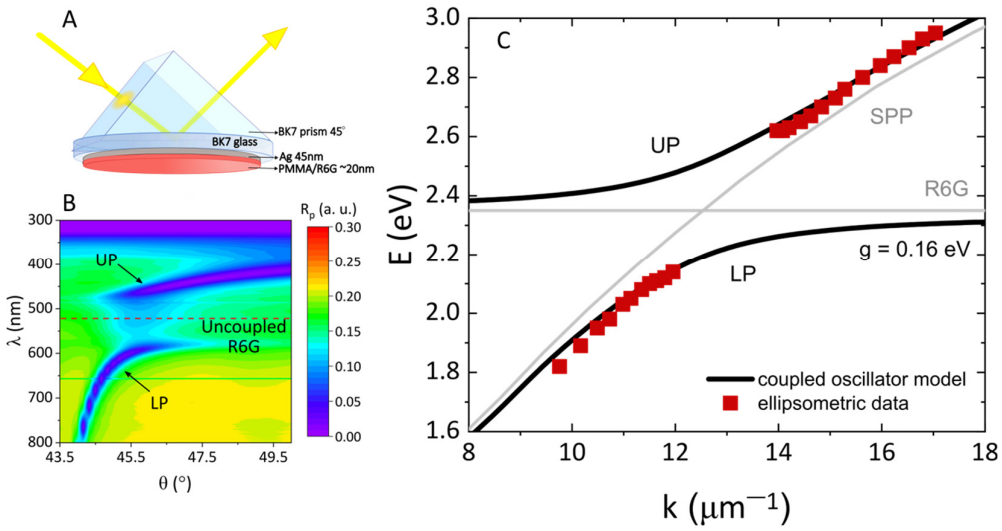

Figure 1. Ellipsometric measurements in TIRE configuration: (**A**) Schematic representation of the TIRE measurement setup using a 45° prism; (**B**) measured dispersion relation of the coupled SPP—R6G structure with observable UP and LP branches and weakly coupled R6G absorption (red dashed line). The modeled dispersion (**C**) relation of strongly coupled SPP—R6G structure, with coupling strength of 160 meV (black lines). The measured dispersion relation follows UP and LP states (red squares). The uncoupled SPP and R6G dispersions are depicted by gray lines.

A custom-built BFP setup was used to investigate polaritonic emission under non-resonant excitation conditions in a reflection-geometry setup (Figure 2). Illumination at normal incidence to the SPP-R6G surface was employed to achieve non-resonant excitation conditions and observe a significant fraction of excitons spontaneously emitting from the exciton reservoir (ER) state. Non-resonant excitation refers to conditions where the excitation laser is detuned from the polaritonic resonance, allowing the excited states to be populated indirectly through the (ER). The ER state consists of excitons that remain weakly coupled after laser excitation and is populated when non-resonant excitation conditions of the polaritonic state are applied. This enables the systems to transition from the ER to the LP state, thereby exciting the polaritonic state indirectly. This is in contrast to resonant excitation, where the polaritonic state is populated directly by the laser excitation. Therefore, to observe emission in both weak and strong coupling regimes, non-resonant excitation should be used [46]. Furthermore, polaritonic states typically exhibit angle-dependent emission, unlike weakly coupled states, enabling angular discrimination between weakly and strongly coupled states under an appropriate incidence angle.

Upon excitation, emitted photons from the SPP-R6G structure were collected by a microscope objective, and the light focused at the BFP of the objective was directed through the first 4f imaging system. Images were formed at the first Fourier plane (FP1), at the focus of L3. Fourier-transformed images of the original intensity distribution at the sample plane were obtained by placing a detector after L5, at the second Fourier plane (FP2), providing wavevector (angle)-dependent information of directional SPP-R6G emission. However, by placing a variable aperture (Thorlabs SM1D12) at FP1, the k-space image can be transformed by filtering the wavevector components, depending on the aperture size and position. By mounting the aperture on a translation stage moving perpendicular to the optical axis, we were able to select different sections of the BFP image, which were sent through the second 4f setup for fluorescence lifetime and intensity distribution analysis.

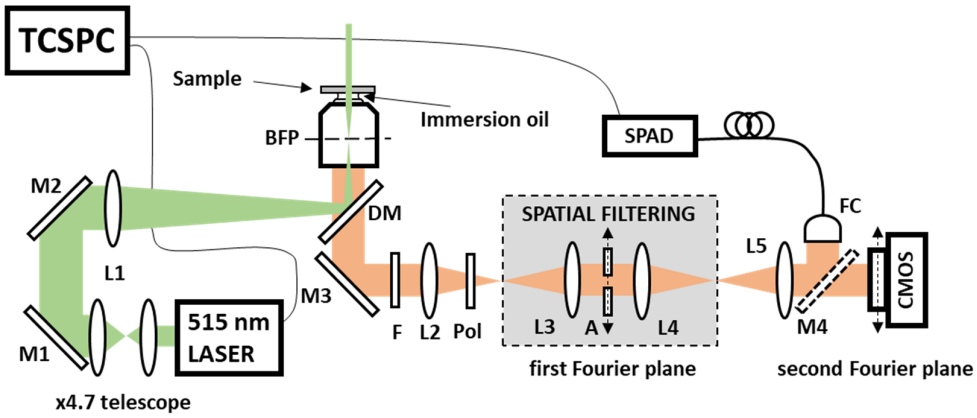

Figure 2. Back focal plane (BFP) microscopy setup with spatial filtering configuration. Fluorescence lifetime measurements are performed using time-correlated single photon counting (TCSPC). Excitation of polaritonic states is achieved using a collimated beam (515 nm) when focused on the BFP of an oil-immersion objective (NA = 1.49) with lens (L1). Emission (orange) is collected from the BFP using two 4f imaging setups (L2–L5). An aperture on a translation stage is inserted at the first Fourier plane to optically filter different emission angles from the BFP. Components: mirrors (M1–M4), lenses (L1–L5), dichroic mirror (DM), long-pass filter (F), polarizer (Pol), aperture (A), fiber coupler (FC).

Back focal plane images reveal angle-dependent emission intensity patterns of R6G fluorescence dye strongly coupled to SPPs (Figure 3). Two images correspond to the emission intensity with the polarizer set at two mutually orthogonal directions. Cross-sections of BFP images taken along the yellow dashed line are depicted in Figure 3C. The emission intensity profile originates from a combination of two main contributors, which can be distinguished as weakly coupled fluorescence and strongly coupled polaritonic emission. Weakly coupled fluorescence, emanating from a collection of R6G molecules within the R6G-SPP structure and remaining in the uncoupled state, appears as a Gaussian emission profile with a full width at half maximum (FWHM) of 33.2°. The excitation laser source is visible as a sharp peak at the center of the BFP.

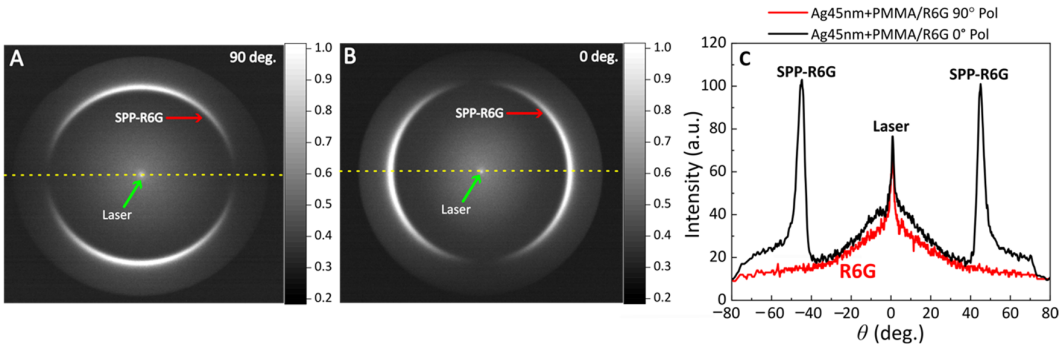

Figure 3. Polarization-dependent angular emission intensity pattern in the BFP with the polarizer set to two orthogonal directions (**A**–**C**) BFP cross-section taken along the yellow dashed line from (**A**,**B**). The sharp peak around 0° correspond to laser leakage through the filters.

Meanwhile, a ring-shaped structure at angles of ±43°, exhibiting an exponential decay profile (Figure 3C), can be attributed to the emission from the strongly coupled state, due to interaction with the SPP mode. In addition to the angular information obtained from BFP images, introducing polarizing optics provides insight into the polarization of the emitted light. Strongly coupled emission from the polaritonic state is highly linearly polarized and can be attenuated by rotating the polarizer in the collection arm (Figure 3C). It is well known that SPPs are excited at the p-polarized light, thus, the polarizer was used

to distinguish between two orthogonal polarizations. This is in contrast to fluorescence in the weak coupling regime, where R6G emission exhibits no polarization dependence. Consequently, the Gaussian intensity peak was seen in both cross-sections (A, red curve in Figure 3C, and B, black curve in Figure 3C).

Comparing the angular emission cross-section of regular R6G fluorescence -depicted as a Gaussian curve in the intensity profile (Figure 3) and taking its ratio with the sharp R6G-SPP peaks provides an approximate percentage of molecules that radiatively decay in weak and strong coupling regimes. A value of 29% was obtained, indicating that nearly 71% of the detected fluorescence stems from polaritonic emission under strong coupling conditions. Therefore, different fluorescence mechanisms can be expected when considering emission from the central part of the BFP versus the sides. Fluorescence lifetime scanning across BFP was performed by placing a variable aperture at FP1 to act as a k-space filter (Figure 4A). When open, the aperture transmits all wavevectors, producing a wide-field BFP image. The acceptance angle of the oil objective was limited by NA = 1.49 (orange dashed line), corresponding to a 157° field of view. Closing the aperture to the minimal permittable size (radius = 0.5 mm) attenuates the wavevector components of the BFP, which fall outside the aperture, effectively filtering the BFP image. Only the wavevectors within the aperture (yellow dashed line) can pass through. When the aperture was closed, the full width half maximum (FWHM) was restricted to ~24°, transmitting only a narrow angular range. This allowed the BFP to be divided into five distinct sections by adjusting the lateral position of the aperture. The corresponding filtered image, collected by a single-photon avalanche detector (SPAD), was sent to the TCSPC unit to measure fluorescence lifetime at different angles of the coupled SPP-R6G sample. The relatively large aperture size limits the resolution for distinguishing individual BFP sections; however, introducing both vertical and lateral shifts to the aperture would enable an array of n × m different BFP sections, where n is the total number of lateral positions and m is the total number of vertical positions. This would increase the number of obtainable BFP sections with corresponding lifetimes. Moreover, a closed aperture with FWHM of ~24° transmits a broad angular range, limiting the ability to resolve features narrower than the aperture's FWHM. This is particularly important when measuring SPP-R6G emission, which has a FWHM of 4.8°. However, analysis of the intensity profile reveals that when the aperture is positioned at (1) or (5), the dominant contribution to the fluorescence decay originates from SPP-R6G, enabling detection of lifetime shortening from emission angles narrower than the aperture's FWHM.

Emission decay profiles (Figure 4B) exhibit distinct fluorescence lifetime across the different sections of the BFP when transitioning from positions (1) → (5). The convolution of the biexponential decay function, described by $\boldsymbol{I(t)} = \boldsymbol{A_1 e^{-(t/\tau_1)}} + (1 - \boldsymbol{A_1})\boldsymbol{e^{-(t/\tau_2)}}$ with the Instrument Response Function (IRF) was performed and fitted to the measured lifetime decay, yielding R^2 = 0.97–0.98. The IRF of the system was limited to ~100 ps. Coefficient $\boldsymbol{A_1}$ corresponds to emitter populations which are close to the metal interface, while $\boldsymbol{A_2}$ represents emitters which are further away and do not interact or only weakly interact with the metal, respectively. Retrieved lifetime data varied when scanned across the BFP image. In particular, the central region (3) of the BFP image shows the longest fluorescence decay, with lifetime values of $\boldsymbol{\tau_1}$ = 0.183 ± 0.001 ns and $\boldsymbol{\tau_2}$ = 2.920 ± 0.068 ns and amplitudes $\boldsymbol{A_1}$ = 0.786 ± 0.001, $\boldsymbol{A_2}$= $(1 - \boldsymbol{A_1})$ = 0.214, respectively. This area collects fluorescence emission from the emitters through the entire thickness of the R6G/PMMA layer. The influence of excitation laser leakage through the filters was minimal when measuring fluorescence lifetime at position (3), due to femtosecond-pulse excitation. Fluorescence at (3) was dominated by emitters farther from the metal interface, as indicated by the increased amplitude parameter $\boldsymbol{A_2}$. Transitioning to either side of the sample,

corresponding to emission at higher angles, results in faster fluorescence lifetimes. At positions (2) and (4), emission dynamics remained in the weak coupling regime, similar to position (3), with lifetime values of τ_1 = 0.106 ± 0.001 ns and τ_2 = 2.494 ± 0.081 ns and with A_1 = 0.969 ± 0.001, A_2 = 0.031. The noticeable shortening of τ_1 at positions (2) and (4) and increased amplitude A_1 from ≈0.79 to ≈0.97 suggests increased quenching of emitters near the metal interface [47]. Differences in the fluorescence decay lifetimes can be attributed to higher detection angles at positions (2) and (4), where fluorescence primarily originates from emitters closer to the metal surface, as indicated by the increased A_1 population. Moreover, differences in emission profiles between positions (3) and (2), (4) may indicate angle-dependent quenching behavior, arising from interference between direct and reflected emission paths, leading to modified emission rates even in the absence of the SPP modes [4]. Meanwhile, the largest change in fluorescence lifetime occurs when transitioning to strongly coupled polaritonic emission at ≈43°. Measurements of the outer SPP-R6G ring at positions (1) and (5) exhibit the fastest decay rate, as compared to the other regions. The detected signal is dominated by the IRF rather than fluorescence from the sample, making the precise retrieval of fluorescence lifetimes from SPP-R6G challenging.

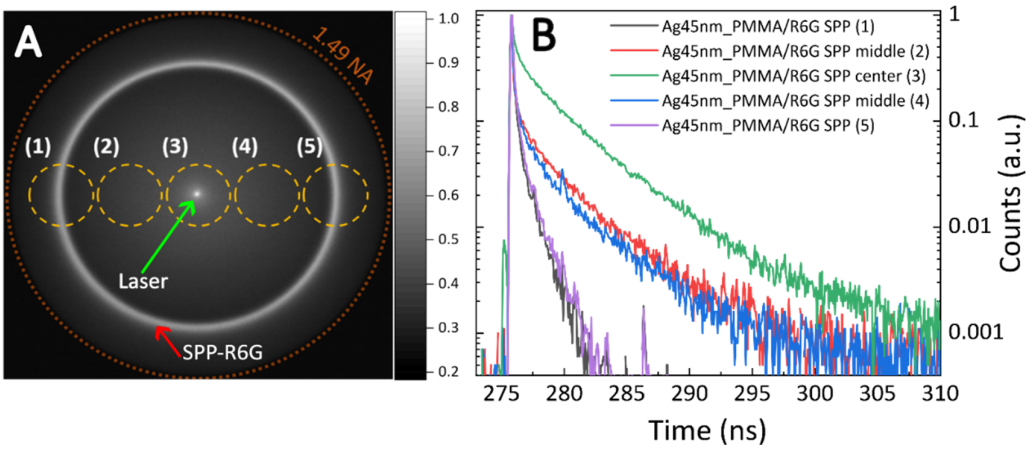

Figure 4. BFP investigation of filtered fluorescence lifetime: (**A**) Strongly coupled SPP-R6G intensity image in the BFP. Yellow circles indicate spatially filtered sections used for fluorescence lifetime measurements. The red circle indicates maximum acceptance angle from which the light can couple into the oil-immersion objective; (**B**) Time-resolved fluorescence decay profiles shown for different sections of the filtered BFP image.

It should be noted that fluorescence decay values approaching the system IRF must be interpreted with caution. It is well known that interaction with the metal layer accelerates radiative transitions to the ground state [4]; however, the exact angular distribution of the intensity pattern is highly dependent on the plasmonic structure at hand. Under non-resonant excitation conditions, the polariton bottleneck effect [48] increases typical polariton lifetimes, bringing them closer to R6G emission rates in a PMMA matrix. Repopulation from the ER to the LP state is limited by slow relaxation times, which in turn slow the radiative decay rates to the ground state [46,49]. It should be noted that the fluorescence decay observed from polaritonic emission at positions (1) and (5) does not capture the full dynamics of the emission process, due to the limitation of the temporal resolution set by the IRF of the system. Nevertheless, this clearly indicates that the lifetimes from plasmon-exciton polaritonic states are much shorter than those of weakly coupled emitters.

Strong coupling dynamics, governed by Rabi oscillations, are expected to appear at tens of femtosecond timescales in plasmonic structures [37], thus placing a limit on the required timing resolution of the measurement setup. Fast energy exchange between upper and lower polariton branches reduces system losses via coherent energy transfer.

However, coupling strength in the strongly coupled regime can also influence the absorption/scattering ratio in highly absorbing nanostructures due to radiative losses, which correspond to the increased scattering through the lower SPP-like polariton branch. The absorption/scattering ratio, in turn, affects the coupling conditions [50,51].

3. Materials and Methods

Thin films of poly(methyl methacrylate) (PMMA) doped with R6G (PMMA-R6G) were prepared by dissolving PMMA (1×10^{-5} mol/L; 0.0367 g/L) and R6G (25×10^{-3} mol/L) separately in ethanol. The solutions were mixed in a 2:1 volume ratio (PMMA:R6G) to obtain the coating solution. Films were deposited onto metallic substrates via spin-coating at 3000 rpm for 30 s, resulting in uniform layers approximately 20 nm thick. The structure under investigation consisted of a thin (170 μm) glass coverslip (CS) with a uniform silver layer (Ag) sputtered on top, where the metal thickness was ~45 nm. A solution of R6G molecular fluorescent dye in PMMA was spin-coated on top of the metallic layer.

The dispersion characteristics of the Ag/PMMA-R6G structures were measured using spectroscopic ellipsometry in a total internal reflection geometry. A RC2 ellipsometer (J.A. Woollam, Lincoln, TX, USA), equipped with dual rotating compensators and a xenon lamp (spectral range: 210–1700 nm), was employed. The optical signal was recorded using a CCD detector (Edmund Optics, Mainz, Germany). Samples were optically coupled to a BK7 prism (45° angle) using index-matching oil. Measurements were performed at angles of incidence ranging from 43° to 50° relative to the surface normal. The angles reported in Figure 1 represent calculated values at the BK7/metal interface.

Excitation of the sample was performed using epifluorescence microscopy configuration (EPI) with incident angles normal to the surface. A femtosecond laser source Femtolux 3 (EKSPLA, Vilnius, Lithuania) with variable pulse duration set at 216 fs and a central wavelength at 515 nm was used to excite the sample in the strong coupling regime. Laser repetition rate was set to 1 MHz. The coverslip with a multilayered structure was placed on high numerical aperture oil objective (NA 1.49) and connected using index-matching oil to enable efficient collection of plasmonic near field at the metal surface. Additionally dichroic filter FITC (Thorlabs, Lübeck, Germany) and a long pass filter at λ = 550 nm were used to filter out λ = 515 nm laser and leave the emission from the polaritonic state. Polarization analysis was performed by introducing a polarizer in the collection arm of the BFP imaging setup. Excitation was carried out with a semi-collimated light beam with divergence half-angle of ~3°, achieved by placing a focusing lens in front of the microscope objective to focus the incoming beam onto the BFP of the objective. Photon count rate was maintained below 10^4 counts per second during the fluorescence lifetime experiment to avoid detector saturation effects.

4. Conclusions

To conclude, polaritonic fluorescence lifetime measurements were performed in a modified BFP imaging configuration. The addition of spatial filtering in the Fourier plane permitted angular discrimination of fluorescence lifetimes within the BFP imaging setup, which is crucial for investigating nanophotonic devices. Fluorescence lifetime decay properties at different emission angles were examined for SPP-R6G samples in the strong coupling regime. For the experiments, a plasmonic structure (Ag) with R6G excitons was fabricated, and the TIRE method was used to evaluate the dispersion relations. The coupled oscillator provided a reasonable fit and revealed a coupling strength of 160 meV. The optical configuration exploiting BFP filtering was used to select different sections of the BFP image and measure corresponding lifetime values in the strong coupling regime. By introducing a lateral shift to the aperture, it was shown that intensity images in the BFP originate from a

collection of different fluorescence lifetime values, indicating multiple decay pathways for emission at different angles.

The method was verified using strongly coupled SPP-R6G system with a directional emission pattern. It was shown that for strongly coupled SPP-R6G samples, the observed lifetime was dominated by the IRF at emission angles of ≈43°, indicating fast transition rates. Fluorescence decay dynamics transitioned to slower decay rates, with lifetimes of 0.1 ns at positions (2) and (4) and 0.18 ns at position (3), whenever emission was collected at different angles. The angle-dependent fluorescence lifetime mapping provides evidence of collective effects. The observed faster decay in the strong coupling regime directly reflects the presence of polaritonic eigenstates with varying degrees of collective character (analogous to Dicke sub-radiance). This research is particularly relevant for devices that exploit collective oscillations with directional emission and controlled excited-state dynamics, such as quantum polaritonic devices and single-photon emitters. The ability to map fluorescence lifetimes at specific angles offers a deeper insight into the decay pathways in these systems, which is critical for optimizing their performance and properties.

Author Contributions: Conceptualization, P.J. and Z.B.; methodology, P.J., J.A. and E.S.; software, E.S. and V.Ž.; validation, P.J., J.A. and E.S.; formal analysis, P.J., J.A. and E.S.; investigation, P.J., J.A. and E.S.; resources, V.Ž. and Z.B.; data curation, P.J. and J.A.; writing—original draft preparation, P.J., J.A., E.B.-V. and Z.B.; writing—review and editing, P.J., J.A., E.B.-V., I.P. and Z.B.; visualization, P.J.; supervision, Z.B.; project administration, Z.B.; funding acquisition, E.B.-V., I.P. and Z.B. All authors have read and agreed to the published version of the manuscript.

Funding: This project has received funding from the Research Council of Lithuania (LMTLT), agreement No S-PD-24-65.

Data Availability Statement: Data underlying the results presented in this paper are not publicly available at this time but may be obtained from the authors upon reasonable request.

Conflicts of Interest: The authors declare no conflicts of interest.

References

1. Di Martino, G.; Sonnefraud, Y.; Tame, M.S.; Kéna-Cohen, S.; Dieleman, F.; Özdemir, Ş.K.; Kim, M.S.; Maier, S.A. Observation of Quantum Interference in the Plasmonic Hong-Ou-Mandel Effect. *Phys. Rev. Appl.* **2014**, *1*, 034004. [CrossRef]
2. Kreinberg, S.; Grbešić, T.; Strauß, M.; Carmele, A.; Emmerling, M.; Schneider, C.; Höfling, S.; Porte, X.; Reitzenstein, S. Quantum-Optical Spectroscopy of a Two-Level System Using an Electrically Driven Micropillar Laser as a Resonant Excitation Source. *Light Sci. Appl.* **2018**, *7*, 41. [CrossRef] [PubMed]
3. Huang, L.; Xu, L.; Woolley, M.; Miroshnichenko, A.E. Trends in Quantum Nanophotonics. *Adv. Quantum Tech.* **2020**, *3*, 1900126. [CrossRef]
4. Wei, H.; Yan, X.; Niu, Y.; Li, Q.; Jia, Z.; Xu, H. Plasmon–Exciton Interactions: Spontaneous Emission and Strong Coupling. *Adv. Funct. Mater.* **2021**, *31*, 2100889. [CrossRef]
5. Novotny, L. *Principles of Nano-Optics*, 2nd ed.; Cambridge University Press: Cambridge, UK, 2012; ISBN 978-1-107-00546-4.
6. Xu, X.; Luo, Q.; Wang, J.; Song, Y.; Ye, H.; Zhang, X.; He, Y.; Sun, M.; Zhang, R.; Shi, G.; et al. Large-Field Objective Lens for Multi-Wavelength Microscopy at Mesoscale and Submicron Resolution. *Opto-Electron. Adv.* **2024**, *7*, 230212. [CrossRef]
7. Zhu, H.; Luo, J.; Dai, Q.; Zhu, S.; Yang, H.; Zhou, K.; Zhan, L.; Xu, B.; Chen, Y.; Lu, Y.; et al. Spatiotemporal Hemodynamic Monitoring via Configurable Skin-like Microfiber Bragg Grating Group. *Opto-Electron. Adv.* **2023**, *6*, 230018. [CrossRef]
8. Marschner, S.R.; Westin, S.H.; Lafortune, E.P.F.; Torrance, K.E. Image-Based Bidirectional Reflectance Distribution Function Measurement. *Appl. Opt.* **2000**, *39*, 2592. [CrossRef]
9. Wang, Y.; Yang, T.; Tuominen, M.T.; Achermann, M. Radiative Rate Enhancements in Ensembles of Hybrid Metal-Semiconductor Nanostructures. *Phys. Rev. Lett.* **2009**, *102*, 163001. [CrossRef]
10. Backer, A.S.; Moerner, W.E. Extending Single-Molecule Microscopy Using Optical Fourier Processing. *J. Phys. Chem. B* **2014**, *118*, 8313. [CrossRef]
11. Lieb, M.A.; Zavislan, J.M.; Novotny, L. Single-Molecule Orientations Determined by Direct Emission Pattern Imaging. *J. Opt. Soc. Am. B* **2004**, *21*, 1210. [CrossRef]

12. Schneider, L.M.; Esdaille, S.S.; Rhodes, D.A.; Barmak, K.; Hone, J.C.; Rahimi-Iman, A. Direct Measurement of the Radiative Pattern of Bright and Dark Excitons and Exciton Complexes in Encapsulated Tungsten Diselenide. *Sci. Rep.* **2020**, *10*, 8091. [CrossRef] [PubMed]
13. Schuller, J.A.; Karaveli, S.; Schiros, T.; He, K.; Yang, S.; Kymissis, I.; Shan, J.; Zia, R. Orientation of Luminescent Excitons in Layered Nanomaterials. *Nat. Nanotech.* **2013**, *8*, 271–276. [CrossRef] [PubMed]
14. Gao, Y.; Weidman, M.C.; Tisdale, W.A. CdSe Nanoplatelet Films with Controlled Orientation of Their Transition Dipole Moment. *Nano Lett.* **2017**, *17*, 3837–3843. [CrossRef] [PubMed]
15. Cueff, S.; Berguiga, L.; Nguyen, H.S. Fourier Imaging for Nanophotonics. *Nanophotonics* **2024**, *13*, 841–858. [CrossRef]
16. Hinamoto, T.; Hamada, M.; Sugimoto, H.; Fujii, M. Angle-, Polarization-, and Wavelength-Resolved Light Scattering of Single Mie Resonators Using Fourier-Plane Spectroscopy. *Adv. Opt. Mater.* **2021**, *9*, 2002192. [CrossRef]
17. Seo, C.; Shim, J.E.; Kim, C.; Lee, E.; Choi, G.H.; Yoo, P.J.; Yi, G.R.; Kim, J.; Kim, T.T. Back-Focal Plane Scanning Spectroscopy for Investigating the Optical Dispersion of Large-Area Two-Dimensional Photonic Crystal Fabricated by Capillary Force Lithography. *Curr. Appl. Phys.* **2024**, *65*, 47–52. [CrossRef]
18. Dang, N.H.M.; Zanotti, S.; Drouard, E.; Chevalier, C.; Trippé-Allard, G.; Amara, M.; Deleporte, E.; Ardizzone, V.; Sanvitto, D.; Andreani, L.C.; et al. Realization of Polaritonic Topological Charge at Room Temperature Using Polariton Bound States in the Continuum from Perovskite Metasurface. *Adv. Opt. Mater.* **2022**, *10*, 2102386. [CrossRef]
19. Genco, A.; Cruciano, C.; Corti, M.; McGhee, K.E.; Ardini, B.; Sortino, L.; Hüttenhofer, L.; Virgili, T.; Lidzey, D.G.; Maier, S.A.; et al. *K* -Space Hyperspectral Imaging by a Birefringent Common-Path Interferometer. *ACS Photonics* **2022**, *9*, 3563–3572. [CrossRef]
20. Engay, E.; Huo, D.; Malureanu, R.; Bunea, A.I.; Lavrinenko, A. Polarization-Dependent All-Dielectric Metasurface for Single-Shot Quantitative Phase Imaging. *Nano Lett.* **2021**, *21*, 3820–3826. [CrossRef]
21. Zhao, H.; Wang, C.; Lyu, C.; Zhao, X.; Sun, B.; Gao, Y. Efficient Lasing Enabled by Enhanced Light-Matter Interaction through Aligned Nanoplatelets in Resonators. *ACS Photonics* **2024**, *11*, 4559–4566. [CrossRef]
22. DeCrescent, R.A.; Brown, S.J.; Schlitz, R.A.; Chabinyc, M.L.; Schuller, J.A. Model-Blind Characterization of Thin-Film Optical Constants with Momentum-Resolved Reflectometry. *Opt. Express* **2016**, *24*, 28842. [CrossRef] [PubMed]
23. Akselrod, G.M.; Argyropoulos, C.; Hoang, T.B.; Ciracì, C.; Fang, C.; Huang, J.; Smith, D.R.; Mikkelsen, M.H. Probing the Mechanisms of Large Purcell Enhancement in Plasmonic Nanoantennas. *Nat. Photon.* **2014**, *8*, 835–840. [CrossRef]
24. Zhou, W.; Liu, J.; Zhu, J.; Gromyko, D.; Qiu, C.; Wu, L. Exceptional Points Unveiling Quantum Limit of Fluorescence Rates in Non-Hermitian Plexcitonic Single-Photon Sources. *APL Quantum* **2024**, *1*, 016110. [CrossRef]
25. Su, Y.; Lu, H.; Li, D.; Wang, C.; Zhao, J. Strong Photoluminescence Enhancement from a WS_2 Atomic Layer Integrated on a Metallic Nanogroove Array with Intermediate Plasmon–Exciton Coupling. *Photon. Res.* **2024**, *12*, 3006. [CrossRef]
26. Manuel, A.P.; Kirkey, A.; Mahdi, N.; Shankar, K. Plexcitonics–Fundamental Principles and Optoelectronic Applications. *J. Mater. Chem. C* **2019**, *7*, 1821–1853. [CrossRef]
27. Lakowicz, J.R.; Malicka, J.; Gryczynski, I.; Gryczynski, Z. Directional Surface Plasmon-Coupled Emission: A New Method for High Sensitivity Detection. *Biochem. Biophys. Res. Commun.* **2003**, *307*, 435–439. [CrossRef]
28. Wang, J.; Zhai, Y.; Pan, X.; Xu, L.; Li, Z.; Cao, S.; Li, Y. Surface Plasmon Coupled Directional Emission for Integrated Fluorescence-Raman Biodetection: A Proof-of-Concept Study. *Chem. Methods* **2022**, *2*, e202100089. [CrossRef]
29. Purcell, E.M. Spontaneous Emission Probabilities at Radio Frequencies. In *Confined Electrons and Photons*; Burstein, E., Weisbuch, C., Eds.; NATO ASI Series; Springer: Boston, MA, USA, 1995; Volume 340, p. 839. ISBN 978-1-4613-5807-7.
30. Törmä, P.; Barnes, W.L. Strong Coupling between Surface Plasmon Polaritons and Emitters: A Review. *Rep. Prog. Phys.* **2015**, *78*, 013901. [CrossRef]
31. Kim, Y.; Barulin, A.; Kim, S.; Lee, L.P.; Kim, I. Recent Advances in Quantum Nanophotonics: Plexcitonic and Vibro-Polaritonic Strong Coupling and Its Biomedical and Chemical Applications. *Nanophotonics* **2023**, *12*, 413–439. [CrossRef]
32. Flick, J.; Rivera, N.; Narang, P. Strong Light-Matter Coupling in Quantum Chemistry and Quantum Photonics. *Nanophotonics* **2018**, *7*, 1479–1501. [CrossRef]
33. Anulytė, J.; Žičkus, V.; Bužavaitė-Vertelienė, E.; Faccio, D.; Balevičius, Z. Strongly Coupled Plasmon-Exciton Polaritons for Photobleaching Suppression. *Nanophotonics* **2024**, *13*, 4091–4099. [CrossRef] [PubMed]
34. Herrera, F.; Spano, F.C. Cavity-Controlled Chemistry in Molecular Ensembles. *Phys. Rev. Lett.* **2016**, *116*, 238301. [CrossRef] [PubMed]
35. Hutchison, J.A.; Schwartz, T.; Genet, C.; Devaux, E.; Ebbesen, T.W. Modifying Chemical Landscapes by Coupling to Vacuum Fields. *Angew. Chem. Int. Ed.* **2012**, *51*, 1592–1596. [CrossRef]
36. Novotny, L. Strong Coupling, Energy Splitting, and Level Crossings: A Classical Perspective. *Am. J. Phys.* **2010**, *78*, 1199–1202. [CrossRef]
37. Vasa, P.; Wang, W.; Pomraenke, R.; Lammers, M.; Maiuri, M.; Manzoni, C.; Cerullo, G.; Lienau, C. Real-Time Observation of Ultrafast Rabi Oscillations between Excitons and Plasmons in Metal Nanostructures with J-Aggregates. *Nat. Photonics* **2013**, *7*, 128–132. [CrossRef]
38. Schlawin, F.; Kennes, D.M.; Sentef, M.A. Cavity Quantum Materials. *Appl. Phys. Rev.* **2022**, *9*, 011312. [CrossRef]

39. Dicke, R.H. Coherence in Spontaneous Radiation Processes. *Phys. Rev.* **1954**, *93*, 99–110. [CrossRef]
40. Gold, D.C.; Huft, P.; Young, C.; Safari, A.; Walker, T.G.; Saffman, M.; Yavuz, D.D. Spatial Coherence of Light in Collective Spontaneous Emission. *PRX Quantum* **2022**, *3*, 010338. [CrossRef]
41. Biteen, J.S.; Pacifici, D.; Lewis, N.S.; Atwater, H.A. Enhanced Radiative Emission Rate and Quantum Efficiency in Coupled Silicon Nanocrystal-Nanostructured Gold Emitters. *Nano Lett.* **2005**, *5*, 1768–1773. [CrossRef]
42. Dowran, M.; Butler, A.; Lamichhane, S.; Erickson, A.; Kilic, U.; Liou, S.; Argyropoulos, C.; Laraoui, A. Plasmon Enhanced Quantum Properties of Single Photon Emitters with Hybrid Hexagonal Boron Nitride Silver Nanocube Systems. *Adv. Opt. Mater.* **2023**, *11*, 2300392. [CrossRef]
43. Mollet, O.; Huant, S.; Dantelle, G.; Gacoin, T.; Drezet, A. Quantum Plasmonics: Second-Order Coherence of Surface Plasmons Launched by Quantum Emitters into a Metallic Film. *Phys. Rev. B* **2012**, *86*, 045401. [CrossRef]
44. Li, N.; Han, Z.; Huang, Y.; Liang, K.; Wang, X.; Wu, F.; Qi, X.; Shang, Y.; Yu, L.; Ding, B. Strong Plasmon–Exciton Coupling in Bimetallic Nanorings and Nanocuboids. *J. Mater. Chem. C* **2020**, *8*, 7672–7678. [CrossRef]
45. Anulytė, J.; Bužavaitė-Vertelienė, E.; Vertelis, V.; Stankevičius, E.; Vilkevičius, K.; Balevičius, Z. Influence of a Gold Nano-Bumps Surface Lattice Array on the Propagation Length of Strongly Coupled Tamm and Surface Plasmon Polaritons. *J. Mater. Chem. C* **2022**, *36*, 13234–13241. [CrossRef]
46. Jurkšaitis, P.; Anulytė, J.; Spalinskaitė, E.; Bužavaitė-Vertelienė, E.; Žičkus, V.; Banevičius, D.; Kazlauskas, K.; Balevičius, Z. Plasmon–Exciton Polaritonic Emission Lifetime Dynamics under Strong Coupling. *Nanophotonics* **2025**, *14*, 2485–2493. [CrossRef] [PubMed]
47. Anger, P.; Bharadwaj, P.; Novotny, L. Enhancement and Quenching of Single-Molecule Fluorescence. *Phys. Rev. Lett.* **2006**, *96*, 113002. [CrossRef]
48. Mony, J.; Hertzog, M.; Kushwaha, K.; Börjesson, K. Angle-Independent Polariton Emission Lifetime Shown by Perylene Hybridized to the Vacuum Field Inside a Fabry–Pérot Cavity. *J. Phys. Chem. C* **2018**, *122*, 24917–24923. [CrossRef]
49. Cho, I.; Kendrick, W.J.; Stuart, A.N.; Ramkissoon, P.; Ghiggino, K.P.; Wong, W.W.H.; Lakhwani, G. Multi-Resonance TADF in Optical Cavities: Suppressing Excimer Emission through Efficient Energy Transfer to the Lower Polariton States. *J. Mater. Chem. C* **2023**, *11*, 14448–14455. [CrossRef]
50. Nishijima, Y.; To, N.; Balčytis, A.; Juodkazis, S. Absorption and Scattering in Perfect Thermal Radiation Absorber-Emitter Metasurfaces. *Opt. Express* **2022**, *30*, 4058. [CrossRef]
51. Pelton, M.; Storm, S.D.; Leng, H. Strong Coupling of Emitters to Single Plasmonic Nanoparticles: Exciton-Induced Transparency and Rabi Splitting. *Nanoscale* **2019**, *11*, 14540–14552. [CrossRef]